Journal of The
Electrochemical Society

Unraveling the Complex Temperature-Dependent Performance and Degradation of Li-Ion Batteries with Silicon-Graphite Composite Anodes

To cite this article: Max Feinauer *et al* 2024 *J. Electrochem. Soc.* **171** 110506

Journal of The Electrochemical Society, 2024 **171** 110506

Unraveling the Complex Temperature-Dependent Performance and Degradation of Li-Ion Batteries with Silicon-Graphite Composite Anodes

Max Feinauer,[1] Margret Wohlfahrt-Mehrens,[1,2] Markus Hölzle,[1] and Thomas Waldmann[1,2,3,z]

[1]*Zentrum für Sonnenenergie- und Wasserstoff-Forschung Baden-Württemberg (ZSW), 89081 Ulm, Germany*
[2]*Helmholtz Institute Ulm for Electrochemical Energy Storage (HIU), 89081 Ulm, Germany*
[3]*Institute of Surface Chemistry and Catalysis, Ulm University, 89081 Ulm, Germany*

Competing effects of graphite and Si result in a complex temperature dependent performance and degradation of Li-ion batteries with Si-graphite composite anodes. This study examines the influence of varying the Si content (0 to 20.8 wt%) in Si-graphite composite anodes with consistent areal capacity and N/P ratio in full cells containing NMC622 cathodes. One hundred pilot-scale double-layer pouch cells were built and cycle aged in the temperature range from −10 to 55 °C. Electrochemical characterization demonstrated that increasing Si contents enhance capacity and mitigate internal resistance at low temperatures. On the other hand, high Si contents decrease charge-discharge energy efficiency and cycle life, particularly at elevated temperatures. Post-mortem analysis of aged electrodes, including physico-chemical characterization (scanning electron microscopy, energy-dispersive X-ray analysis, thickness measurements) and cell reconstruction revealed significant solid electrolyte interphase growth and increased loss of active material in anodes with high Si content. The optimum temperature for longest cycle life as derived from Arrhenius plots decreased from 30 °C for graphite anodes to 10 °C for cells with moderate Si content up to 5.8 wt%. These findings allow the design of optimized cells by balancing the Si content versus operating temperature in order to achieve lowest cell aging.
 [DOI: 10.1149/1945-7111/ad8d0d]

Manuscript submitted August 19, 2024; revised manuscript received October 2, 2024. Published November 11, 2024.

Supplementary material for this article is available online

The growing demand for high-performance batteries with high specific capacity is currently served with silicon (Si) as promising alternative anode material in Li-ion batteries. Pure Si offers approximately ten times the specific capacity of commonly used graphite and can also improve fast charging capability, particularly under low temperature conditions where safety-critical Li plating is a concern.[1,2] However, the advantages of Si are accompanied by significant drawbacks, such as low electric conductivity and sluggish Li-ion diffusion.[3,4]

Unlike graphite, which allows Li to intercalate into its host structure, Si forms an alloy with Li, resulting in a substantial volume expansion of almost 300 % at the highest alloying level at room temperature.[5,6] Furthermore, this alloying process is correlated with a voltage hysteresis during charging and discharging.[5,6] This voltage hysteresis complicates state-of-charge (SOC) estimation based on cell-voltage recording and reduces overall energy efficiency of such cells.[7,8] Moreover, the continuous expansion and contraction of Si during battery cycling can cause damage to the electrode structure by cracking and pulverization of Si particles.[9–12] This damage results in the loss of electrical connectivity of the particles, which is equivalent to the loss of anode active material (LAAM).[3] Additionally, electrolyte decomposes at the newly exposed electrode surfaces after particle and solid electrolyte interphase (SEI) cracking and a new and continuously thicker SEI layer accumulates.[13] This further causes capacity loss due to loss of Li inventory (LLI) and LAAM due to the loss of the electrical connection because of the isolating nature of the SEI.[6]

Both, pulverization and the correlated continuous SEI growth lead to strong irreversible electrode volume expansion. This could further lead to a deformation of the jelly roll in cylindrical cells, resulting in increased capacity loss, higher internal resistances and in the worst case to internal short circuits.[14,15] In addition to cyclic aging, Si containing cells are also known to have an increased calendar aging rate due to the instability of the passivating SEI layer on the Si particles.[13,16,17]

Various strategies have been employed to address these challenges of Si anodes in Li-ion batteries. The use of Si nanoparticles reduces the absolute volume expansion per particle.[5,6,18,19] However, it decreases the volumetric energy density and increases the surface area, leading to more electrolyte decomposition and thus LLI.[5,6,18,19] Another very common way is incorporating Si with well-established graphite in composite electrodes to overcome the intrinsic problems of pure Si electrodes.[20,21] In Si-graphite composite electrodes, the volume expansion is limited, the amount of inactive materials such as conductive agents and binder can be reduced, and the surface area, where electrolyte decomposition occurs, is reduced.[3,6,11]

In Si-graphite composite anodes, a mix of Si and graphite electrochemical characteristics is observed. Si is lithiated and delithiated at higher potentials compared to graphite and has different kinetics for the insertion and extraction of Li.[3,22–24] Thus, during charging and vice versa during discharging in Si-graphite composite electrodes, there is the tendency of Si to be lithiated first.[23,25] Graphite is lithiated at a later stage when the potential of the anode gets lower.[23,25] This knowledge helps improve the cycle life of Si-graphite composite electrodes by limiting the used capacity of Si by avoiding in particular low SOC where Si is predominately active.[1,14,26–30] However, high charging rates and low temperatures can alter the lithiation order of graphite and Si due to different kinetic activation barriers of both components.[31,32] The diffusion coefficient of Li in Si is approximately three orders of magnitude lower than in graphite at room temperature.[33]

While the specific energy of Si-graphite composite electrodes increases linearly with Si content,[21] volumetric energy density does not due to the strong volume expansion of Si in the lithiated state. As a consequence, the maximum state-of-the-art Si-content in commercial applications today is in the range of 5–8 wt%.[5,13,24] Further increasing the Si content decreases the columbic efficiency and the irreversible capacity loss over time and cycles due to extensive SEI growth.[2,34,35] Strategies like carbon coating around Si nanoparticles improve cycle life by stabilizing the SEI.[36] Furthermore, pre-lithiation is a way to compensate for irreversible Li losses during formation, though scaling up pre-lithiation processes is challenging.[3,18,24,37]

[z]E-mail: thomas.waldmann@zsw-bw.de

Temperature plays a crucial role in battery performance and aging. High temperatures enhance performance by improving conductivity, diffusivity, and the exchange current density between solid and liquid phase, but also accelerate aging by increasing the reaction rate of parasitic side reactions such as SEI growth.[1,32,38] At lower temperatures, cyclic aging could lead to Li plating, which reacts with electrolyte on its surface and forms electrically disconnected "dead Li".[39,40] Evaluating the aging rates in an Arrhenius plot often leads to a V-shape curve, with an optimum temperature corresponding to the longest cycle life at the minimum.[41–46] While the temperature dependent aging of Li-ion batteries with graphite anodes is well understood,[41,43–47] the temperature dependent degradation mechanisms of Si-containing anodes are less clear and are barely studied so far.[29,30,32,38,48–50] This applies particularly for Si-graphite composite anodes at temperatures in the range above and below room temperature.

In previous publications, pouch full cells with Si-graphite composite anodes with 0 wt% Si (pure graphite), 3.0 wt% Si, 3.5 wt% Si, 5.8 wt% Si and 20.8 wt% Si and nickel-manganese-cobalt oxide cathode (NMC622) cathodes were built and analyzed.[2,16,21,51] In order to ensure comparability and to investigate the effect of increasing Si content in the anode, these cells had—within the error bar of manufacturing—very similar N/P ratios. The anode coatings also had very similar areal capacities, porosities and tortuosities. Thus, electrodes with higher Si content are thinner. The NMC622 cathode is known for both its high specific energy and cycling stability,[52,53] which is crucial for investigating aging effects on the anode side. Cathode capacities were adjusted to compensate for irreversible capacity losses during formation, resulting in thicker cathodes in cells with higher Si content.

In this study, we utilize pilot-scale electrodes from one manufacturing batch to investigate the influence of temperature in a wide range from −10 °C to 55 °C on cell performance and aging. We investigate electrochemical properties (capacity, direct current internal resistance (DCIR), energy efficiency, differential voltage analysis (DVA), 3-electrode full cells with Li reference electrode), create Arrhenius plots of the cyclic aging rate and carry out post-mortem analyses, including scanning electron microscopy (SEM) and energy dispersive X-ray spectroscopy (EDX) of cross-sectioned anodes, thickness measurements, and the reconstruction of aged cells into coin half cells.

Experimental

Electrode and pouch cell manufacturing.—The electrodes for the pouch full cells were manufactured in-house on a pilot coating line. Five different anode active materials (Iopsilion, China) with different ratios of graphite and Si were selected: 0 wt% Si (pure graphite), 3.2 wt% Si, 3.7 wt% Si, 6.2 wt% Si, and 23.1 wt% Si. The anode coatings were prepared using the active material, CMC (Timcal, Switzerland) and SBR (Zeon, Japan) binder, and SuperC65 conductive additive (Nippon paper Industries, Japan) in a weight ratio of 94:2:2:2 and an adjusted weight ratio of 90:3:3:4 for the SiG20.8 anode with the highest Si content. This results in a total Si content in the anode of 0 wt% (graphite), 3.0 wt% (SiG3.0), 3.5 wt% (SiG3.5), 5.8 wt% (SiG5.8), and 20.8 wt% (SiG20.8). The slurry was coated with a width of 80 mm on both sides of a smooth 10 μm copper foil (JX Nippon). The mass loading was adjusted for the different Si contents to result in the same areal capacity for all coatings. Calendering was conducted at a roll temperature of 40 °C to a target density of 1.3 g cm^{-3}. The characteristic values of the anode are summarized in Table I.

Similarly, the N-methyl pyrrolidone (NMP) based cathode electrode was prepared using NMC622 cathode active material (BASF, Germany), PVDF binder (Solvay, Belgium), and carbon black and graphite conductive additive (both Timcal, Switzerland) in a weight ratio of 94:2:2:2. The slurry was coated on a 15 μm aluminum foil with varying loadings to obtain the same N/P ratio of the full cells for anodes with different irreversible losses during formation. The cathode electrodes were calendered at a roll temperature of 100 °C to a target density of 3.2 g cm^{-3}. Further details regarding the electrodes and their manufacturing process can be found in the work of Flügel et al.[2]

A double-sided coated anode with an area of 26 cm^2 and two single-sided coated cathodes with an area of 24 cm^2 were assembled to bilayer pouch cells in a dry room (dew point < −60 °C). A Celgard 2325 separator was used. The pouch cells were filled in an argon-filled glovebox ([O_2] < 0.1 ppm, [H_2O] < 0.1 ppm, MBraun) with 900 μl of 1 M $LiPF_6$ in EC:DEC (3:7 wt%) with 2 wt% VC for the graphite cells and 10 wt% FEC for the Si containing cells (Gotion, USA). Different electrolytes were chosen for the cells with and without Si in order to create the most stable SEI for each component. It is therefore evident that FEC is capable of forming a beneficial, stable and highly Li-ion conductive SEI in both Si and graphite anodes.[3,5,10,13,49,54–59] Furthermore, VC is known to improve the cycle life of graphite anodes, particularly by effectively stabilizing the SEI.[59–61]

Formation and cyclic aging.—The formation and cyclic aging of the batteries was conducted using CTS systems (BaSyTec, Germany). A slight pressure was applied to the cells during the formation and cyclic aging by means of bracing in custom holders. The pouch cells were operated in a voltage range from 3.0 V to 4.2 V.

After 20 h of soaking time, the formation procedure was initiated at room temperature. The formation procedure comprised three cycles of constant current (CC) charging at a rate of 0.1 C, followed by a constant voltage (CV) charging with a cut-off current of 0.05 C and CC discharging at 0.1 C.

Following the formation, the 100 cells were transferred to climate chambers (Vötsch, Germany) with ambient temperatures of −10 °C, 0 °C, 10 °C, 20 °C, 25 °C, 30 °C, 35 °C, 45 °C, and 55 °C. A minimum of two cells per condition were tested as can be seen in Table II. The following errors are calculated using the standard deviation of all cells tested under identical conditions. The cells underwent cyclic aging through continuous CC-CV charging to the upper cut-off voltage (4.2 V) at a rate of 0.5 C and a cut-off current of 0.05 C, followed by CC discharging at 0.5 C until the lower cut-off voltage (3.0 V). The capacity of the third discharge step of the formation procedure was used to define the C-rate. A wait time of 10 min after each charging and discharging step ensured uniform temperature conditions. A check-up cycle at 0.1 C was performed every 50 cycles at the aging temperature. The cyclic aging was conducted until the capacity dropped below 80 % of its initial capacity at a certain temperature.

The initial voltage drop at the beginning of each 0.5 C discharge step (100 % SOC) was used to determine the DCIR by measuring the voltage drop within the first 10 s and dividing this by the current.

3-electrode full cells with Li reference electrode.—3-electrode PAT full cells with a Li reference electrode (EL-Cell, Germany) were assembled in a glove-box using the same electrodes as in the pouch cells. This methodology allows to track the potentials of individual electrodes vs Li/Li^+ in particular during the charging process at varying temperatures for the anodes with different Si content.

Single-side coated 18 mm diameter electrodes were punched from the electrodes. For the assembly of the PAT full cells, a double-layer separator (180 μm PP fiber Freudenberg FS2226 E and 38 μm PE membrane Lydall Solupor 5P09B) was used. The cells were filled with 100 μl of the same electrolyte as described above for the pouch cells.

Following a 20 h soaking period, three 0.1 C formation cycles (CC-CV charging cut-off current: 0.05 C) were performed in a CTS (Germany) climate chamber at 25 °C using a Maccor (USA) Series 400 cell test system. The capacity of the third discharge step of the formation procedure was used to establish the C-rate for the further tests, ensuring a comparable current density to that of the original

Table I. Summary of anode characteristics. Data is taken from Flügel et al.[2].

	Unit	Graphite	SiG3.0	SiG3.5	SiG5.8	SiG20.8
Si content in active material	wt%	0	3.2	3.7	6.2	23.1
total Si content	wt%	0	3.0	3.5	5.8	20.8
mass loading	mg cm^{-2}	8.7	7.7	7.4	6.9	5.3
areal capacity	mAh cm^{-2}	3.11	3.16	3.18	3.20	3.40
N/P ratio in full cell		1.10	1.11	1.10	1.09	1.13
porosity	%	42.4	43.5	44.1	42.7	42.9
tortuosity	%	7.92	6.08	7.57	7.04	6.71

Table II. Number of pouch cells for the different investigated anodes, cycled at a certain temperature. A total of 100 cells were investigated.

	Temperature								
Anode	−10 °C	0 °C	10 °C	20 °C	25 °C	30 °C	35 °C	45 °C	55 °C
graphite	0	3	2	2	2	2	2	3	2
SiG3.0	2	4	2	2	2	2	2	2	2
SiG3.5	2	2	3	2	2	0	2	3	2
SiG5.8	3	2	2	3	2	2	2	4	2
SiG20.8	4	4	3	2	2	0	3	2	2

pouch cell. The 0.5 C test cycles were conducted successively at 25 °C, 20 °C, 10 °C, 0 °C, and −10 °C, with the cell discharged and charged under the same conditions as for the cyclic aging procedure. An intermediate 0.2 C cycle was conducted at 25 °C between each test cycle.

Cell opening and post-mortem characterization.—New, i.e. immediately after formation, and aged pouch cells with a state-of-health (SOH) of about (80 ± 5) % were opened and the harvested electrodes were used to assemble coin half cells with Li counter electrode. In addition, the negative electrodes of selected aged cells were used to prepare cross-sections for SEM.

The pouch cells were fully discharged to 3.0 V in five steps at a C/32 current before being disassembled in an argon-filled glove box. The harvested electrodes were washed three times for 1 min in anhydrous DMC (≥99 %, Sigma-Aldrich). Following this procedure, the electrodes were dried under vacuum conditions at 3 mbar for 2 h. A micrometer screw gauge was used to measure the thickness of the washed electrodes.

Cross-sections of the washed anodes were prepared using a Hitachi (Japan) IM4000Plus broad-beam argon ion milling system with a beam voltage of 5 kV. Air exposure could not be avoided during sample preparation. A LEO 1530 VP SEM (Zeiss, Germany) equipped with a Gemini field emission column was used to characterize the cross-sections. Measurements were taken at an acceleration voltage of 5 kV using an Edward-Thornley SE detector. An accelerating voltage of 10 kV was used for the EDX mappings.

Reconstruction of pouch cells into coin half cells.—The harvested electrodes from the cell opening were used to build a total of 93 coin half cells with a Li counter-electrode. While the original pouch cells already contained two single-side coated cathodes, there is only one double-side coated anode, which cannot be used directly in the 3-electrode setup. Therefore, one side of the coating was removed by laser ablation.[62] During laser ablation, the anodes were exposed to a dry room atmosphere (dew point < −60 °C).

Electrodes with a diameter of 12 mm were punched from the harvested single-sided coated electrodes. Together with two layers of 16 mm GF/A separator (Whatman, UK) and a 16 mm Li chip as counter-electrode, CR2032 coin cells were assembled. The coin cells were filled with 150 µl of the same electrolyte as previously used in the pouch cells.

The formation of the coin cells was performed after 12 h of soaking time by cycling three cycles at 0.1 C (CV cut-off current: 0.05 C). A uniform capacity of 3.0 mAh was assumed for all cells, based on the 125 mAh of a new pouch cell. The anode half cells were operated in a voltage range between 1.5 V and 0.01 V and the cathode half cells in a voltage range between 3.0 V and 4.3 V.

Results and Discussion

Temperature dependent performance.—The performance of Li-ion battery cells, including parameters such as available capacity, internal resistance, and energy and coulombic efficiency, is significantly influenced by temperature.[49,63] These temperature dependent characteristics are affected by various factors, including the materials used, electrode composition and structure, and even cell geometry. This section will specifically examine how the Si content in the anode impacts the temperature dependent performance of the battery cells.

The effect of temperature on the available discharge capacity of new cells is shown for five different Si containing anodes with same areal capacity in Fig. 1a. It is evident that low temperatures significantly reduce the available capacity. This reduction in capacity is attributed to decreased Li-ion conductivity in the electrolyte and SEI, increased charge-transfer resistances, and limited solid state diffusivity within the active materials.[64] Low temperatures also lead to a decrease in cell voltage with higher overpotentials, further lowering the usable energy content of the battery cell.

The electrode loading for the cells were designed to ensure that all cells achieve the same capacity at 25 °C and 0.1 C. However, even at a discharge rate of 0.5 C, significant differences in the available capacity at 25 °C were observed. When discharging at 0.5 C and 0 °C, the graphite cell delivers only 74 % of its rated capacity at 25 °C with 0.1 C. In contrast, the cell with the highest Si content (SiG20.8) retains 87 % of its capacity, indicating that the higher discharge potential of Si helps to maintain capacity at low temperatures. The cells with a medium Si content follow the trend and lie between the graphite cells and the SiG20.8 cells. In Si-graphite composites, the Si delays the decrease in anode potential, further improving the graphite capacity utilization.[38]

In addition to the composition of the active material, the electrolyte and its additives can significantly influence the

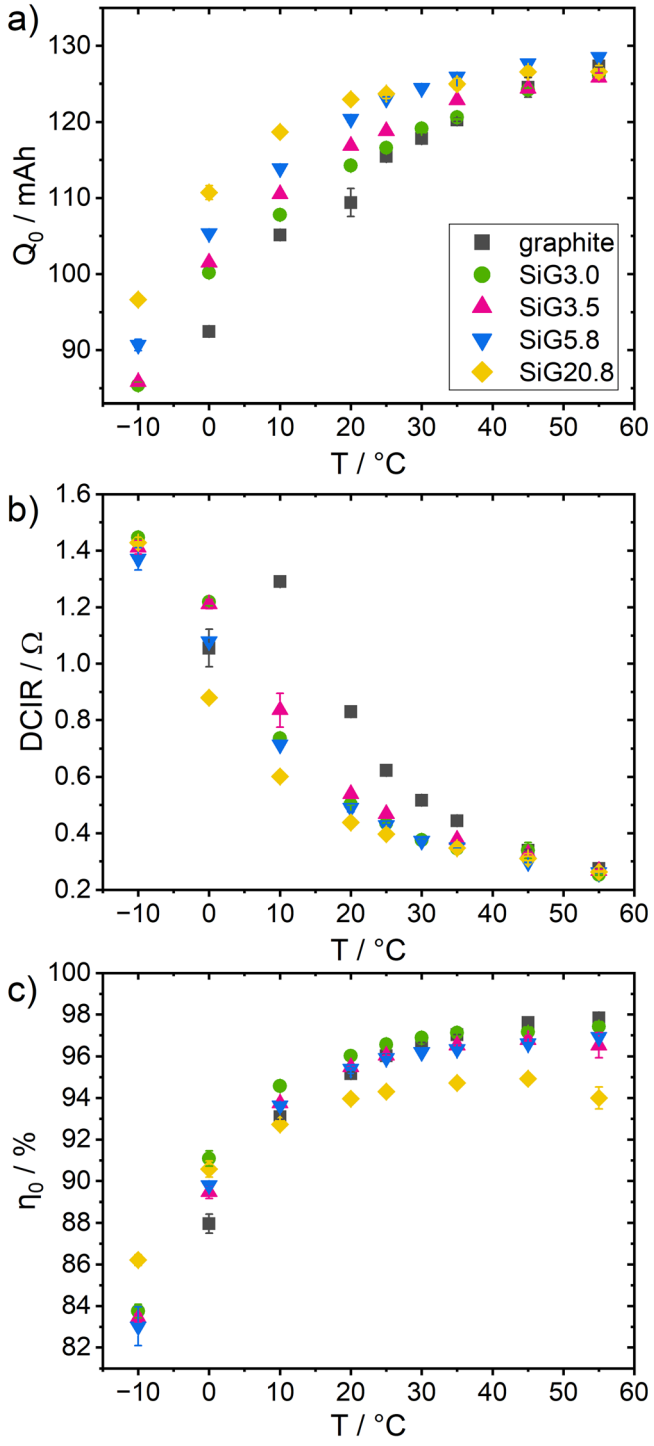

Figure 1. Temperature dependent performance of different Si contents in the anode in pouch cells. (a) Discharge capacity of the first cycle Q_0 of the aging process at 0.5 C, (b) DC internal resistance of new cells, and (c) energy efficiency η_0 of the first 0.5 C aging cycle.

temperature dependent capacity.[65] Electrolytes with FEC additive are known to increase the capacity of cells with Si containing anodes.[48] Since the electrolyte composition is consistent for all Si containing cells in this study, this effect can be excluded from consideration. Nevertheless, despite the observed correlation between higher Si content and enhanced capacity retention at low temperatures, it is likely that the electrolyte additive exerts an additional influence in the graphite cells.

The temperature dependent DCIR and energy efficiency, as shown in Figs. 1b and 1c, are closely linked to the temperature dependent capacity. Increased temperatures reduce internal resistances, primarily due to enhanced Li-ion mobility in electrodes and electrolyte. Additionally, the lower resistance of thinner electrodes, particularly in cells with a higher Si content in the anode,[2] is evident as all other geometrical factors, such as electrode area and cell design, remain constant. Graphite cells appear to be stronger affected by temperature changes, likely due to the used VC containing electrolyte instead of the FEC containing electrolyte in the Si containing cells. Adding up to 15 % FEC to the electrolyte lowers the interfacial resistance due to an improved SEI.[55,57] Interestingly, at temperatures of –10 °C and above 45 °C, the Si content's effect on internal resistance becomes negligible, indicating that other factors dominate the internal resistance. The DCIR of the graphite cells at 0 °C deviates from the expected trend. Although this behavior is consistently reproduced across multiple cells, it is likely due to strong polarization, causing Li deposition on the anode surface rather than Li intercalation into graphite.

High internal resistances lead to increased overpotentials at low temperatures, resulting in higher ohmic losses, which significantly degrade energy efficiency η_0, as shown in Fig. 1c. The pursuit of η_0 is a matter of both sustainably and cost, as well as of the heat produced, which could potentially give rise to significant temperature increases in cells of larger format. At high temperatures, there is a trend toward lower η_0 values with increasing Si content in the anode, particularly pronounced for the SiG20.8 cells. This reduced energy efficiency in cells with high Si content anodes is attributed to the increased voltage hysteresis associated with Si, counteracting the effect of lower internal resistances in cells with increases Si content in the anode. The voltage hysteresis in Si-based anodes is linked to the plastic deformation of the stiff, inorganic SEI around the single particles leading to different stresses during lithiation and delithiation.[7,8,25] However, at low temperatures, the trend of lower energy efficiency with higher Si content in the anode is reversed. Cells with higher Si content exhibit better energy efficiency due to their significantly lower resistance, which leads to reduced overpotentials and overshooting the negative effect of the voltage hysteresis.

As has been demonstrated so far, an increased proportion of Si in the anode is particularly advantageous for the performance at low temperatures. However, as shown on the example of SiG3.0 in Fig. 2, the contribution of the Si component to the total capacity decreases with lower temperature. The initial 0.1 C checkup cycle discharge step at the aging temperature is employed for the DVA in Fig. 2, where characteristic peaks for Si and graphite are identified in consistence with prior publications.[16,21,66] During the charging process and vice versa during discharging, the Si component is mostly lithiated first, followed by the lithiation of the graphite component when the potential of the anode is lower.[23,25,51]

Despite the temperature dependent capacity, which is clearly visible in Figs. 1a and 2, the relative capacity share of the Si component decreases at low temperatures. An increase in temperature from 0 °C to 55 °C results in a 66 % enhancement of the lithiation capacity of Si, while the total capacity increases by only 16 %. This indicates that the Si and graphite components in the composite electrode are utilized in a different manner as a function of temperature. In particular, the contribution of the Si component increases disproportionately with temperature.

These observations demonstrate the complex relationship between temperature and Si content for a constant anode areal capacity, N/P ratio, porosity, and tortuosity on the performance characteristics of Li-ion batteries. Furthermore, the result emphasizes the necessity of optimizing the anode's Si content based on the intended operating temperature range of the battery and the importance of a balanced approach to the Si content of the anode in order to achieve optimal performance across different temperature conditions.

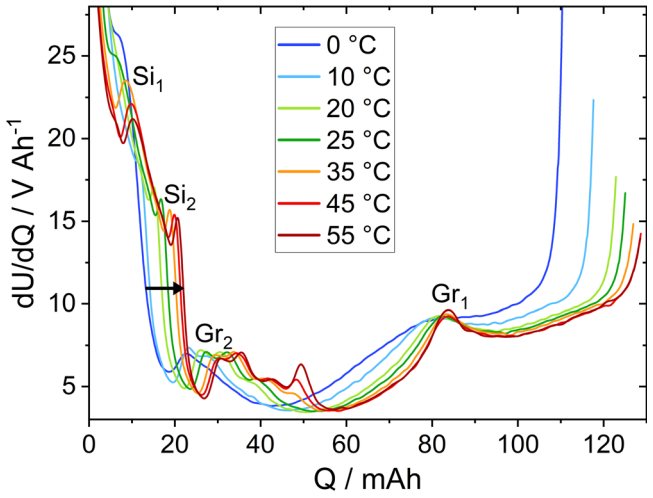

Figure 2. Differential voltage analysis of the initial 0.1 C checkup cycle discharge step as a function of temperature for the SiG3.0 cell. An arrow indicates the increasing capacity of the Si component, as the capacity of the Si related peaks Si_1 and Si_2 and thus of the graphite peak Gr_2 shift towards higher capacities with increasing temperature.

Temperature dependent cyclic aging behavior.—In addition to the aforementioned performance parameters, temperature exerts a significant influence on the degradation mechanisms that occur during storage and particularly during the cycling of battery cells. The degree of aging is typically given by the SOH, which is defined for a certain cycle n by the current capacity Q_n and the maximum capacity Q_{max} by

$$SOH_n = \frac{Q_n}{Q_{max}} \cdot 100\%.$$

Note that Q_{max} is not necessarily the capacity of the first cycle, since in particular for the graphite cells, an initial increase in capacity during the first cycles was observed. Guo et al. explained the increasing capacity during the early aging stage by an increasing graphite capacity due to increased Li-ion diffusion as a result of irreversible d-space increase, which reduces the insertion resistance for the Li-ions.[67]

The SOH of the cells aged at various temperatures for different anode's Si contents is shown in the first column of Fig. 3 (subfigures (a), (d), (g), (j), (m)). For better visibility, only one cell per condition is shown. The full set of aging curves can be found in Figs. S1 to S9 of the supporting information. The step-like shape of some aging curves originates form the frequent checkup cycles, which lead to a partial recovery of the prior capacity loss. A strong effect of temperature on the capacity fading during cyclic aging is evident across all Si contents. The lowest temperature consistently results in the highest capacity fading rate, likely due to strong Li plating. As the performance of the graphite cell at 0 °C was already very poor, no further tests were conducted at −10 °C. Conversely, the optimum temperature, which yields the highest number of cycles until the end-of-life (EOL) at 80 % SOH, varies depending on the anode's Si content. This optimum temperature corresponds to the transition from Li plating at low temperatures to accelerated SEI growth at high temperatures as the dominant aging mechanism, representing the lowest temperature without Li plating.[41–44,46]

The maximum number of observed cycles until the EOL varies significantly by almost a factor of 20 between the cells with a pure graphite anode and those with SiG20.8 anode. While the SiG20.8 cells reached EOL in less than 200 cycles at the optimum temperature of 25 °C, graphite cells maintained an SOH of 85 % after 3,000 cycles at the optimum temperature of 30 °C. Very close to this cycle life, SiG3.0 cells achieved about 2,700 cycles to 84 % SOH at 10 °C. The SiG3.5 and SiG5.8 cells follow the trend of a reduced number of cycles with increased Si content in the anode, achieving 1,800 cycles to 85 % SOH and 1,300 cycles to EOL, respectively, both at 10 °C. This increased capacity loss with increasing Si content indicates mainly a degradation process of the Si component. Most likely, a thick SEI layer accumulates at the surface of the Si-particles during cycling, leading to capacity loss, loss of the electrical connection, and pore clogging.[6,48] The linear capacity loss observed for most aging curves in Fig. 3 indicates that the SEI does not stabilize during cycling, but is likely reformatted within each cycle. Otherwise, similar to calendar aging, the capacity fading and decrease in SEI conductivity would decelerate with the number of cycles in a square-root-like function.[16,68]

Interestingly, when considering solely the first part of the aging process (SOH > 90 %) for the SiG20.8, 10 °C exhibits the lowest capacity fading. However, during further aging, the capacity fading appears to accelerate, making 25 °C to the optimum temperature when considering the whole aging process. One possible explanation for this phenomenon is the deposition of Li on the anodes surface after LAAM, which accelerates the capacity loss.[21]

Cycling of the SiG20.8 cells at 55 °C appears to be problematic, as a significant capacity loss of about 12 % is observed during the first cycle. Despite frequent reports of gassing as a result of side reactions in Si containing anodes,[19,29,69] no significant gas accumulation was overserved after aging across all Si contents, as the pouch bags did not show any ballooning effect.

The second column in Fig. 3 (subfigures (b), (e), (h), (k), (n)) shows the temperature dependent evolution of the DCIR during cyclic aging for the different Si contents in the anode. Across all cells, an increase in DCIR is observed as the SOH decreases. The increase in resistance may result from insulating electrolyte decomposition products and contact loss of particles during cyclic aging, particularly in Si containing cells.[9] This indicates that similar mechanisms are responsible for capacity fading and the growth of internal resistance. For example, a reduction in the electrochemically active area leads to both capacity loss and resistance increase.[27] Else, the growth of a resistive SEI layer consumes cyclable Li and thereby lowers the capacity.[27] Moreover, increased resistance apparently increases the capacity loss further, as larger overpotentials limit complete delithiation.

Besides the clear effect of temperature on the initial DCIR, the evolution of DCIR with aging differs significantly across different temperatures. There is a tendency that the absolute resistance growth as a function of the SOH is the highest around the optimum temperature for cyclic aging. However, when comparing the increase in DCIR normalized to the initial DCIR at a specific temperature, the relative increases in resistance as a function of the SOH are similar at elevated temperatures (⩾20 °C). In particular for the cells with Si containing anodes, the consumption of FEC and other organic electrolyte additives is known to form a resistive SEI layer.[3] Interestingly, the relative increase in DCIR for cells aged at low temperatures (⩽0 °C) is comparatively small. This indicates that Li plating, which typically occurs at these temperatures, is responsible for the accelerated capacity decay, although it does not significantly increase the resistance. Considering the evolution of the DCIR particularly at 10 °C for the SiG3.0, SiG3.5, and SiG5.8 cells, remarkably a non-linear increase in DCIR is observed, indicating different mechanisms leading to resistance increase and to capacity fading. However, this could also be related to the fact that the optimum temperature lies at the transition between Li plating and SEI growth as dominant aging mechanisms.

Comparing the different Si contents in the anode on their resistance evolution in Figs. 3b, 3e, 3h, 3k, 3n, revels a trend of a lower increase in resistance as function of the SOH with increasing Si content. However, it should be considered that the aging is faster in cells with higher Si content, allowing less time for the growth of interfacial resistive layers.

The third column in Fig. 3 (subfigures (c), (f), (i), (l), (o)) represents the temperature dependent energy efficiency during cyclic aging. Across all temperatures and Si contents in the anode of the

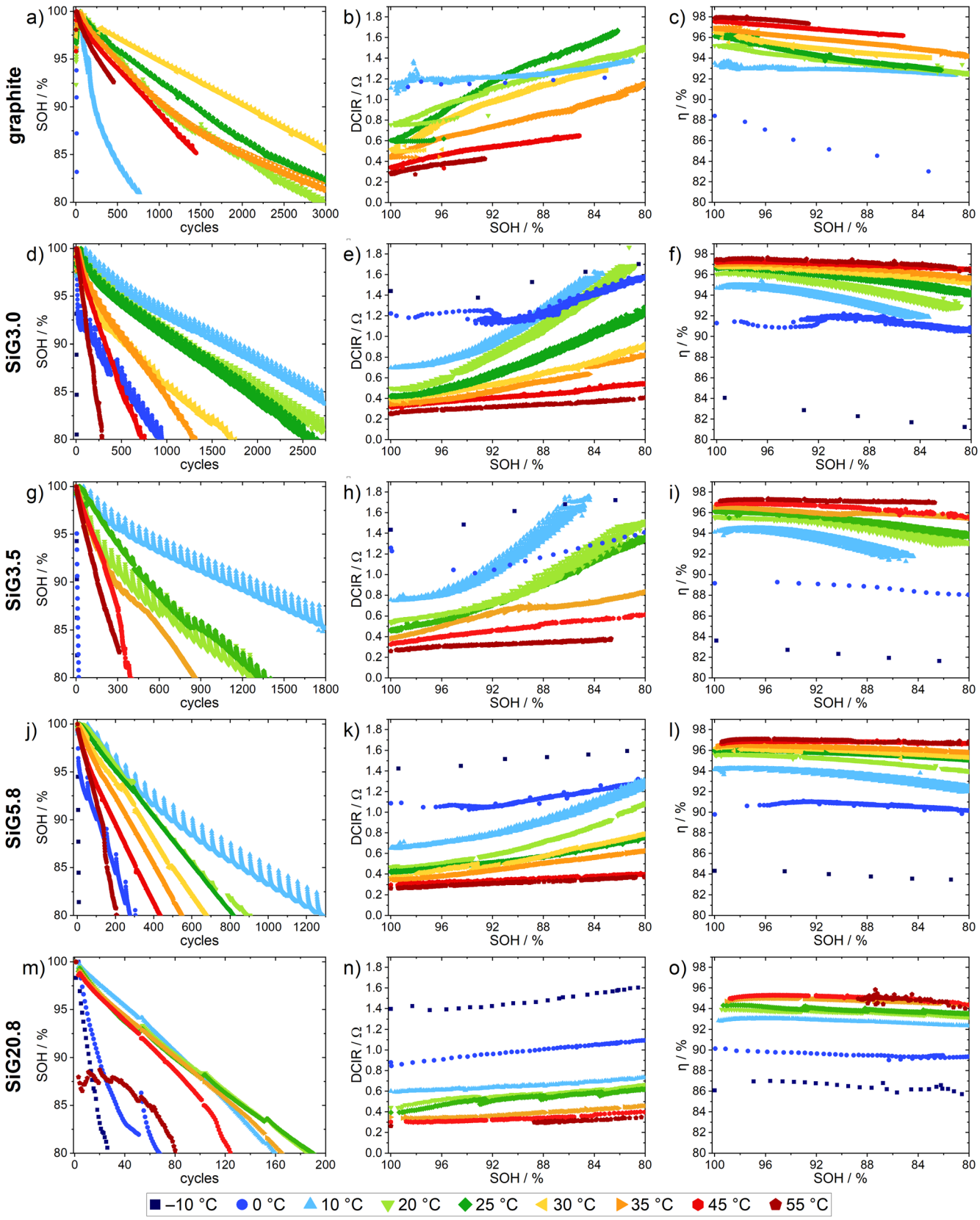

Figure 3. SOH as a function of number of cycles and DCIR and energy efficiency η as a function of SOH for different aging temperatures in the range of −10 °C to 55 °C for the five different electrodes: (a)–(c) graphite, (d)–(f) SiG3.0, (g)–(i) SiG3.5, (j)–(l) SiG5.8, and (m)–(o) SiG20.8. Markedly different scales for the cycling aging must be noted. Scaling for DCIR and energy efficiency is the same for all diagrams. For better visibility, only one cell is shown representatively per condition.

different cells, the energy efficiency declines with ongoing aging, reflecting in particular the increasing resistance. While the relative decline in energy efficiency is smaller at high and low temperatures, in particular around the optimum temperature for the cyclic aging, a more pronounced fading of the energy efficiency is observed. This agrees well with the increased resistance growth around the optimum temperature. The Si content in the anode appears to have only a minor effect on the evolution of the energy efficiency with aging, while the effect of hysteresis manifests as a consistent offset throughout the aging process.

Arrhenius Plots of the cyclic aging rate.—To further evaluate the temperature dependence of the cyclic degradation, Arrhenius plots are a valuable tool.[41,43–46] In accordance with previous publications,[41,43–46] the cyclic aging rate r is defined as the capacity loss in percent SOH per cycle, and is determined by the slope of the linearly fitted aging curves in the first column of Fig. 3. This aging rate can be expressed using an Arrhenius term:

$$r = A \cdot \exp\left(-\frac{E_a}{k_B T}\right),$$

where A is a pre-exponential factor, E_a is the activation energy, k_B is the Boltzmann constant, and T the absolute temperature. According to this equation, the logarithm of the cyclic aging rate r is plotted against the inverse temperature to create an Arrhenius plot.

In the Arrhenius plot for the cyclic aging rate in Fig. 4a, the effect of the Si content in the anode is clearly observable as an offset in the aging rate. This trend of increasing aging rate with increasing Si content is clearly visible in Fig. 4b for high temperatures (≥20 °C), matching well with the results of Moyassari et al.[34] The aging rate increases by nearly a factor of 20, from (0.0053 ± 0.0006) %-SOH/cycle for graphite cells to (0.0960 ± 0.0015) %-SOH/cycle for SiG20.8 cells. As a rough approximation, and for the materials and cycling conditions used here, the Si fraction in the anode correlates linearly with the accelerated aging factor. Nevertheless, it is not solely the influence of cyclic aging, however, also calendar aging is superimposed, which is accelerated with increasing Si content as observed for the same electrodes by Bischof et al.[16] Interestingly, at low temperatures and particularly at −10 °C, the trend in Fig. 4b is reversed and the aging rate decreases with increasing temperature. The 0 °C data point for the cells with 3.5 wt % Si is most likely an outlier.

Typically, Arrhenius plots for the cyclic aging rate of Li-ion battery cells with graphite anode show two distinct linear branches (arranged in a V-shape) for Li plating and SEI growth in the low and high temperature ranges, respectively.[41–46] While a linear, Arrhenius-like behavior of the cyclic aging rate is evident in the high temperature range, the low temperature range and the transitional region in Fig. 4 deviate from a clear linear trend. The longer CV phase at lower temperatures and the concomitant reduced current could have contributed to this discrepancy. Additionally, more intricate aging mechanisms, where the simple model of Li plating and SEI growth is complemented by additional Si-related aging contributions, that are not necessarily temperature dependent, can be assumed. Nevertheless, at least at extreme temperatures, the strongly increasing aging rate with lower temperatures is a strong hint for Li plating as the dominating aging mechanism.[39,40] Higher overpotentials at low temperatures result in a higher degree of lithiation of graphite rather than Si, which is similar to limiting the voltage range beneficial to limit the volumetric expansion of the Si particles, thereby enhancing cycle life.[23,27]

The comparison of the low temperature aging rate for the different Si contents in the anode reveals two clear statements: (i) the superior performance of the cells with the highest Si content (SiG20.8) and (ii) the very poor performance of the graphite cell. Additional Si in the electrode leads to thinner electrodes at the same areal capacity, which reduces polarization and therefore the possibility of Li plating.[2,70] The improved low temperature performance of cells with increasing Si content in the anode agrees well with the findings of Sun et al. who showed a lower capacity fading for cells with up to 15 % Si compared to pure graphite.[38] Berg et al. separately investigated the activation energies for the ionic transport resistance and charge transfer resistance in cells with graphite and Si anodes.[1] The total electrode resistance undergoes a shift from predominantly kinetically limited at low temperatures to transport limited at high temperatures due to the much higher activation energy of the charge transfer resistance, particularly in cells with Si anode and FEC containing electrolyte.[1] In this context, thinner Si electrodes exhibit greater kinetic limitation, whereas thicker graphite electrodes suffer from transport limitations.

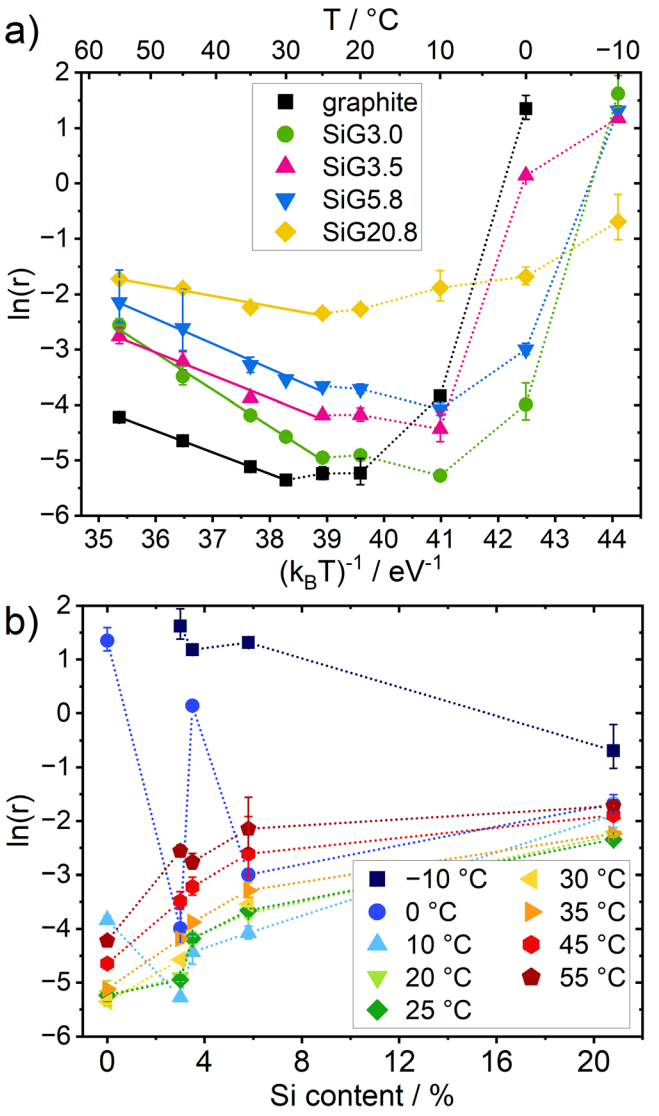

Figure 4. (a) Arrhenius plots of the aging rates r for the cyclic aging at 0.5 C at different temperatures for cells with different Si contents in the anode. Solid lines represent the linear fit in the high temperature range. (b) Logarithm of the aging rate as a function of the Si content in the anode in wt % for various aging temperatures. Dotted lines are drawn to guide the eye.

In addition, the poor low temperature performance of the graphite cells could be partially explained by the use of VC instead of FEC as electrolyte additive due to the poor ionic and electronic conductivity of the formed SEI.[2,71] In contrast, FEC is known to effectively improve the low temperature performance by forming a SEI layer with high ionic conductivity.[56,64,65,72] However, at high temperatures, VC is known to be one of the most effective electrolyte additives to improve the long-term stability, highlighting the trade-off in selecting an appropriate electrolyte additive with good performance across the temperature range.[71]

Table III. Optimum temperature for the cyclic aging with 0.5 C and activation energies of the cyclic aging rate in the high temperature range (25 °C (30 °C for graphite) to 55 °C) with fitting error, observed by linear fitting of the data points in Fig. 4.

Anode	Optimum T/°C	E_a/eV
Graphite	30	0.39 ± 0.01
SiG3.0	10	0.66 ± 0.03
SiG3.5	10	0.41 ± 0.04
SiG5.8	10	0.45 ± 0.03
SiG20.8	25	0.19 ± 0.03

The reduced susceptibility of Li plating in cells with increasing anode Si content also results in a shift in the optimum temperature for cyclic aging. As can be seen in Table III, the optimum temperature decreases from 30 °C for the graphite cell to 10 °C for the cells with 3.0 wt% to 5.8 wt% Si in the anode. The lower the temperature, the slower the Li consuming side reactions occur, resulting in lower aging rates at lower temperatures if the onset of Li plating is not yet reached. This agrees well with the results of Flügel et al. who have shown a trend towards less Li plating in cells with higher Si content in Si-graphite composite anodes with comparable anode areal capacities.[2] However, for the highest Si content in the anode, the optimum temperature is indeed 25 °C, which could be a result of extensive LAAM, eventually leading to Li plating.[21,44] At the same time, the temperature dependence of the SiG20.8 cell is much lower, as shown by the flatter curve of the temperature dependent aging rate in Fig. 4. This indicates that the typically known temperature dependent aging behavior for Li-ion battery cells can be mainly attributed to the graphite component and successively decreases with increasing Si content in the anode.

For the high temperature range of the Arrhenius-plots in Fig. 4, linear fitting of the data points allows the determination of activation energies E_a. We note that the E_a values describe the temperature dependence of the aging rate, but are limited in the interpretation as reaction barriers. In case the E_a values are related to reaction barriers, they should be rather interpreted for the overall reaction. The activation energies are listed in Table III with the corresponding fitting errors. These values ranging from (0.19 ± 0.03) eV to (0.66 ± 0.03) eV are in a similar range to those found in other cyclic aging studies for Li-ion batteries cells.[41,42,44,45,73,74] For calendar aging, which is typically fitted by a square-root of time dependence,[16,68] Bischof et al. observed similar activation energies in the range of (0.27 ± 0.05) eV to (0.48 ± 0.01) eV for the calendar aging rate in cells with the same material as investigated here.[16] Notably, the activation energy in the cell with the highest Si content (SiG20.8) exhibited the lowest value. It is noteworthy that the high temperature branch in the Arrhenius plot in Fig. 4, which was employed for the activation energy fitting, commenced at 30 °C and 25 °C, respectively, for the graphite and SiG20.8 cells. This corresponds to the specific optimum temperature. For the cells with low and medium Si content, a clear deviation from the linear behavior is observed at temperatures below 25 °C, despite the optimum temperature lying at 10 °C. This indicates that there are different contributions to degradation in the temperature range from 10 °C to 25 °C. A linear behavior in the Arrhenius plot for temperatures above the optimum temperature indicates that the dominating degradation mode does not change with temperature. Therefore, it is possible to use elevated temperatures with increased aging rates for accelerated lifetime tests of cells, which can then be extrapolated to lower aging temperatures.

The relationship between the composition of the anode material and the temperature dependent aging rate is presented in Fig. 5. For each investigated temperature, the Si content in the anode, which leads to the lowest aging rate, is shown (bars, left axis of Fig. 5). The corresponding lowest aging rates (r_{min}) are plotted (data points, right axis of Fig. 5) as extracted from the Arrhenius plot in Fig. 4. As illustrated in Fig. 5, at temperatures above 20 °C, the cells with the graphite anode exhibit the lowest aging rate at 0.5 C. At temperatures between 0 °C and 10 °C, the lowest aging rate is observed in cells containing a SiG3.0 anode. The SiG3.0 anode is not susceptible to Li plating at 10 °C, but a lower temperature is related to a lower rate of Li-consuming side reactions such as SEI growth on both graphite and Si particles. Consequently, a similar aging rate is achieved as that of the graphite cell in the range from 20 °C to 30 °C, where no degradation of the Si compound can happen. At −10 °C, the SiG20.8 anode exhibits the best cycle life. At such a low temperature, SEI growth becomes negligible. Conversely, high polarization, which is correlated with Li plating, is improved in Si containing cells compared to graphite cells at low temperatures due to better reaction kinetics.[38,70]

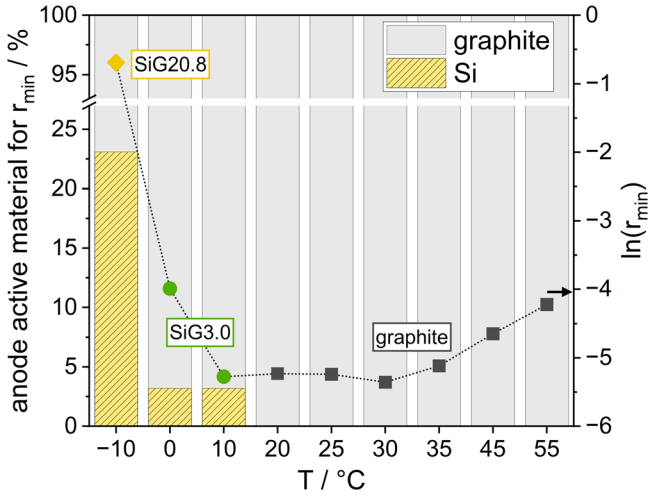

Figure 5. Anode active material composition (ratio of graphite and Si) leading to the lowest cyclic aging rate at a specific temperature for cycling with 0.5 C. The data points mark the corresponding lowest aging rate r_{min}. The style of the data points is consistent with those of the Arrhenius plot in Fig. 4, and the cell names are provided.

In conclusion, the previously described superior low temperature performance of anodes with increased Si content goes along with the improved cyclic aging rate at these low temperatures. Nevertheless, it is unlikely that further increases in Si content will yield additional benefits, as the electrodes will not become significantly thinner and parasitic side reactions limiting the long-term stability will increase. Conversely, at elevated temperatures, a lower Si content is favorable as particularly the degradation of the Si component limits the long-term stability.

Tracking the onset of Li plating via anode reference potential.—The optimum temperature for the cyclic aging is determined by the lowest temperature that prevents Li plating. Li plating gets thermodynamically allowed when the anode potential (U_{anode}) drops below 0 V vs Li/Li^+.[39] Therefore, in order to enhance the cyclic aging rate by identifying the optimum temperature, it is essential to reduce the temperature until the temperature right before the temperature at which the anode potential drops below 0 V vs Li/Li^+ during charging.

Full cells with 3-electrode configuration with an additional Li reference electrode enable the potential of anode and cathode to be monitored separately.[18,44,62,75–77] Consequently, the conditions within the cell that could potentially lead to Li plating are comparable to those observed in pouch full cells. However, it is possible that minor discrepancies may arise due to a different separator and differences in the cell format including factors such as different electrode stack pressure or anode overhang. A good matching of the 3-electrode reference cells and the pouch cells is confirmed by virtually equal voltage curves.

The full cell voltages and simultaneously recorded anode potentials during a 0.5 C CC-CV charging step are shown in Fig. 6 for various temperatures and different Si contents on the anodes. Figure 6f displays the minimal anode potential for all anodes as a function of temperature. It is evident that there is a trend of increasing minimum anode potential with increasing temperature, which corroborates the well-known trend.[44,62] For higher Si contents in anodes with the same anode areal capacity, N/P ratio, porosity, and tortuosity, a trend of higher minimum anode potentials is observed. While the cells with graphite show negative anode potentials for all investigated temperatures ($\leqslant$ 25 °C), SiG5.8, and SiG20.8 show positive minimum anode potentials for temperatures $\geqslant$ 10 °C.

At all temperatures, a clear trend of a lower full cell voltage with increasing Si content in the anode is observed in Fig. 6. This can be attributed to (i) the lower thickness with higher Si content at constant anode areal capacity (leading to less polarization) and (ii) the increasing anode potential, particularly at low SOC (due to presence of more Si). Both effects allow for higher charging rates or lower temperatures to be reached before the voltage drops below 0 V vs Li/Li^+.[1,2] However, the higher anode potential or lower full cell voltage for cells with increased Si content in the anode result in a lower energy content of the cell, despite the capacity of the cell remaining the same. High currents, which lead to large overpotentials, result in a more substantial sloping and smearing out of the graphite lithiation plateaus due to inhomogeneous lithiation of

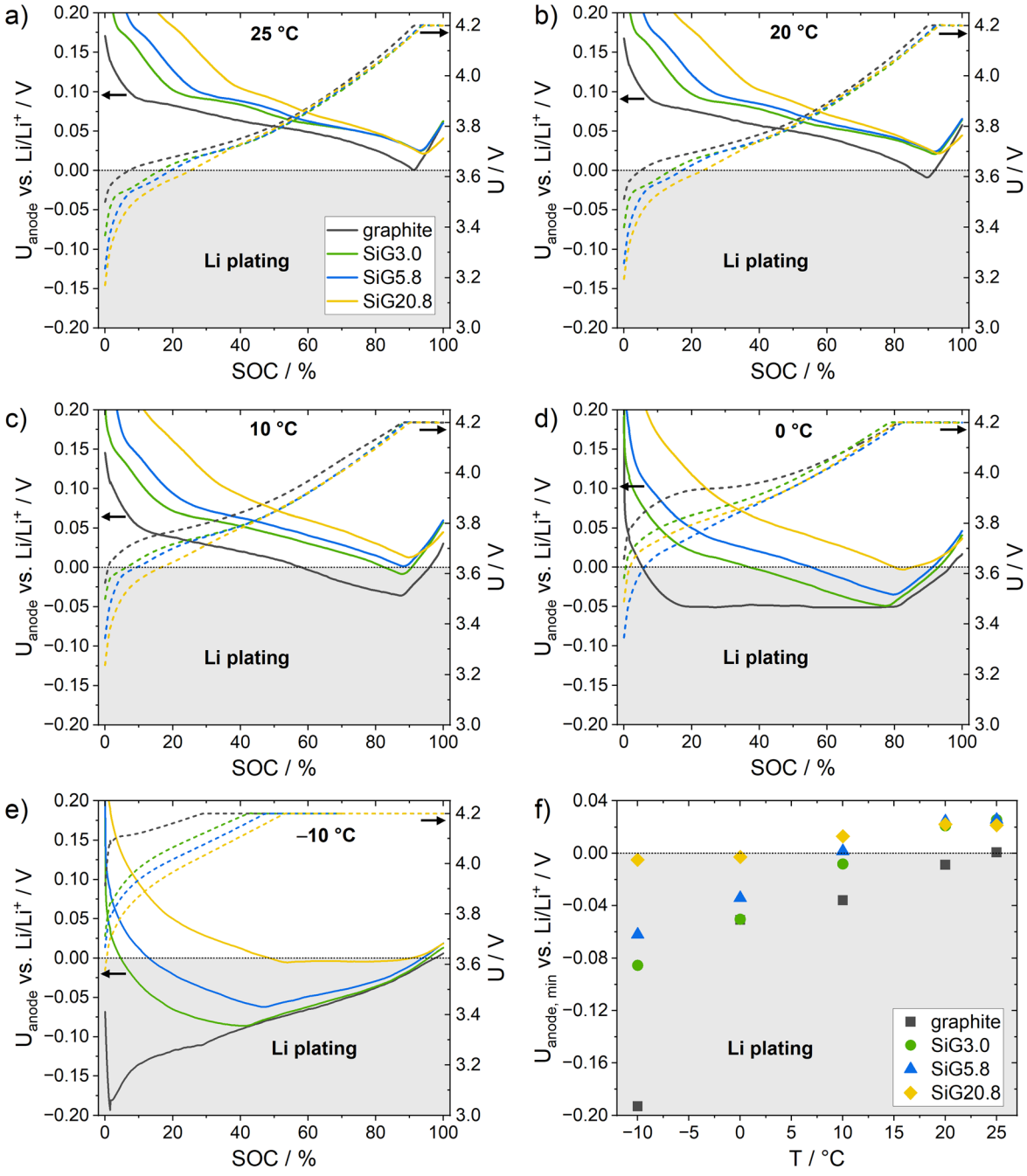

Figure 6. Anode potential vs Li/Li^+ (solid line, left axis) and corresponding full cell voltage U (dashed line, right axis) measured in 3-electrode full cells with Li reference-electrode during charging with 0.5 C at different temperatures: (a) 25 °C, (b) 20 °C, (c) 10 °C, (d) 0 °C, and (e) −10 °C for different Si contents in the anode. (f) Minimal anode potential for different cells as a function of temperature. The grey area below the black dotted line marks anode voltages < 0 V vs Li/Li^+, where Li plating is thermodynamically favored.

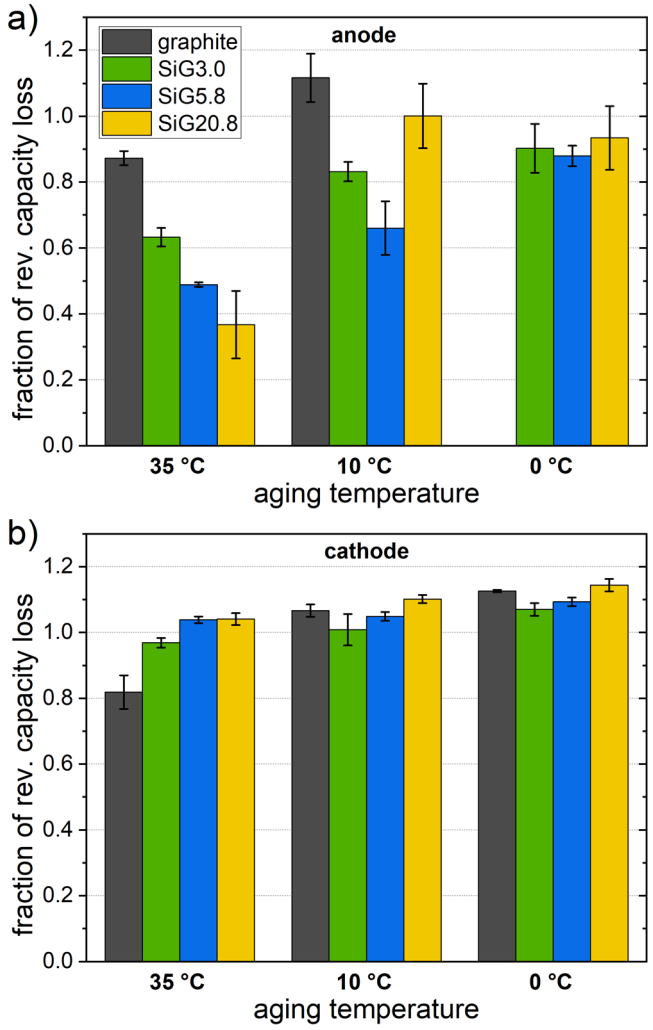

Figure 7. Fraction of reversible capacity loss φ of the total capacity loss determined by coin half-cell measurements of (a) anodes and (b) cathodes from pouch cells with different Si content in the anode, aged at different temperatures. Three coin cells were measured and averaged per condition, resulting in a total of 93 coin cells.

the anodes.[1,78] As shown in Fig. 6a, these plateaus are not even visible at 25 °C.

At 20 °C and 25 °C, the anode potential curves for different Si contents in Figs. 6a and 6b are very close together, particularly at high SOC, where Li plating predominately occurs. However, the graphite potential curve differs from those of the other Si-contents, which is likely a consequence of utilizing a VC-containing electrolyte instead of an FEC-containing one. At lower temperatures, the discrepancies become more pronounced, most likely due to the thinner electrodes in case of higher Si contents, which reduce the ionic resistance and lead to decreased overpotentials. At 0 °C and above, the duration of the CV phase is similar for all Si contents. However, at −10 °C, a clear trend emerges for a shorter CV phase with increasing Si content, likely due to reduced overpotentials.

At 25 °C and above, none of the anode potential curves exhibits a drop below 0 V vs Li/Li^+ during the 0.5 C charging process, indicating the absence of Li plating during cyclic aging. At 10 °C, only the cells with the graphite anode exhibits a significant decline in the anode potential curve below 0 V vs Li/Li^+, which corresponds with the accelerated aging rate for the graphite cell as shown in Fig. 4. At 0 °C, the anode potentials of the SiG3.0 and SiG5.8 cells clearly drop below 0 V vs Li/Li^+, respectively. This is further amplified at −10 °C, indicating the onset of Li plating for the SiG3.0 and SiG5.8 cells around 10 °C which is consistent with the aging data (Fig. 4 and Table II). As shown in Fig. 6e, at −10 °C, charging of the graphite cell becomes problematic due to the presence of huge overpotentials. In strong contrast, the anode potential of the cell with the highest Si content in the anode, SiG20.8, does not exhibit a notable decline below 0 V vs Li/Li^+ even at −10 °C.

Another method for detecting Li plating is by examining the discharge voltage curve. A voltage plateau at the beginning of the discharge step indicates stripping of reversibly plated Li.[79–81] Such a stripping discharge voltage plateau is detected for the graphite cell at 0 °C and below. For the SiG3.0 and SiG5.8 cells, a Li stripping plateau in the discharge voltage curve is observed only at −10 °C. For the SiG20.8 cells, no evidence of Li plating is detectable in the voltage curve even at −10 °C. This is consistent with the results of the anode potential in Fig. 6e and the only slightly increased aging rate in Fig. 4.

In conclusion, the anode potential curves at different temperatures confirm the previously observed trend of decreasing Li plating onset temperatures with increasing Si content in the anode. This is consistent with the findings of Flügel et al., who reported a shift in the critical C-rate in the same cells.[2] Nevertheless, minor discrepancies in the observed onset of Li plating for the 3-electrode measurements (Fig. 6) and the Arrhenius plot (Fig. 4a) may be attributed to factors such as different setups and the incorporation of overlapping aging mechanisms in the aging rate of the Arrhenius plot. Furthermore, it is likely that the minimum in the Arrhenius plot is not precisely determined due to discrete temperature steps, but rather closely approached.

Aging analysis via cell reconstruction into half cells.—DVA is frequently applied to distinguish between different aging mechanisms.[16,21,32,44,66,82] However, particularly in the aged state, the smearing out and broadening of peaks represents a significant limitation of DVA for the analysis of degradation.[28] Reconstructing aged pouch cells into coin-half cells with a Li counter electrode is a valuable and comprehensive method for identifying the underlying degradation mechanisms.[83,84]

The Li counter electrode in the half-cell with the harvested electrode provides sufficient new cyclable Li for a complete lithiation of the electrode. If cyclable Li has been lost during the previous aging process and is responsible for the capacity loss, this can be reversed by the Li counter electrode. Consequently, the capacity fraction regained in the reconstructed cell can be attributed to LLI as a degradation mechanism during cyclic aging. Conversely, if the capacity of the reconstructed cell does not recover with new cyclable Li, it can be assumed that LAAM is the driving degradation mechanism, as the storage capability of the electrode appears to be irreversibly damaged during aging.

As a baseline for the evaluation of the aged cells, a reconstruction of new cells was performed immediately after formation. New and aged cells were treated equally, thus excluding, for example, stresses related to cell opening and reconstruction. The fraction of the reversible capacity loss φ is given by the fraction of capacity regained in the reconstructed coin cell and the total capacity loss. This is calculated by

$$\varphi = \frac{Q_{\text{aged}} - Q_{\text{new}} \cdot \text{SOH}}{Q_{\text{new}} - Q_{\text{new}} \cdot \text{SOH}} = \frac{Q_{\text{aged}} - Q_{\text{new}} \cdot \text{SOH}}{Q_{\text{new}} \cdot (1 - \text{SOH})},$$

where Q_{aged} is the capacity of the coin cell with an aged electrode and Q_{new} the capacity of the reconstructed coin cell with electrodes from a new cell. The use of the SOH of the pouch cells prior to the reconstruction allows to relate the capacity of the full cell to the coin cell. The average fraction of the reversible capacity loss for three coin cells, with corresponding standard deviation, is plotted in Fig. 7 for anodes and cathodes. It should be noted that the error bars are particularly large for the SiG20.8 cell, due to the fragile aged electrode. A reconstruction of the anode of the graphite cell after 0 °C aging was not possible due to extensively plated Li on the electrode surface.

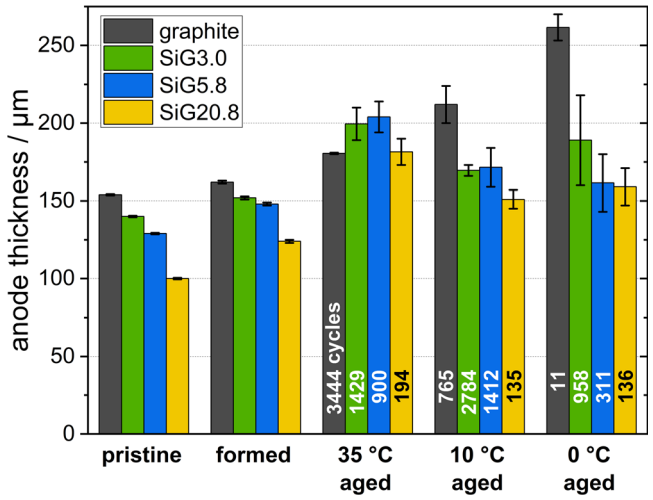

Figure 8. Total thickness of double-sided coated anodes with different Si content before cell manufacturing (pristine), after formation, and after aging at 35 °C, 10 °C, and 0 °C. The figures in the bars of the aged cells display the number of cycles at cell opening.

Figure 7a illustrates the fraction of reversible capacity loss of the anodes with different Si content after aging. For aging at 35 °C, a clear trend towards lower reversible capacity losses, i.e. LAAM, with increasing Si content is revealed. For the highest Si content, approximately two-thirds of the capacity loss can be attributed to LAAM, while LAAM contributes only approximately 12 % to the capacity loss in the graphite cell. Consequently, it can be concluded that for cyclic aging at 35 °C, LAAM is largely correlated with a loss of the Si component.

At an aging temperature of 10 °C and below (Fig. 7a), LAAM does not play a significant role in the total capacity loss of the graphite and SiG20.8 cells, as these cells demonstrate a fully reversible capacity loss, indicating LLI. However, it is important to note that the increasing capacity of the graphite cells during the initial cycles, which was previously attributed to the anode, leads to an underestimation of Q_{new}. This is particularly evident at 10 °C, where the fraction of the reversible capacity loss is $\varphi > 1$. Conversely, the SiG3.0 and SiG5.8 cells still exhibit significant degradation by LAAM at 10 °C. At 0 °C, all cell types show similar degradation, largely dominated by LLI.

These results align well with those presented in Fig. 4, as aging dominated by Li plating increases LLI. Aging conditions without Li plating lead to LAAM as driving degradation factor, particularly in cells with increased Si content in the anode. Kirkaldy et al. attributed the increasing proportion of LAAM of the Si component at elevated temperatures to increased SEI growth, which further triggers particle cracking due to the large concentration gradients in particles with a thick SEI.[27] However, the results shown in Fig. 2, indicate a temperature dependent usage of the Si and graphite component. In particular, at low temperatures, the reduced usage of the Si-component is beneficial for its long-term stability, as the volume expansion during cycling is limited by a lower lithiation degree, resulting in less LAAM.

Figure 7b illustrates the fraction of reversible capacity of the cathodes, showing that under most condition, the values φ are >1. Since the anodes were not pre-lithiated, the loadings of the cathodes were oversized to compensate for the irreversible Li losses during formation and to obtain consistent N/P ratios.[2] This is particularly visible for cells with increasing Si content in the anode, as they suffer from higher irreversible losses during formation.[2] A clearly notable deviation appears as increased irreversible capacity loss at 35 °C, in particularly in the graphite cell. This is likely related to the extensive number of cycles of the cell, leading to minor aging effects in the cathode. A comparison between cells aged at 0 °C and 10 °C reveals a slightly higher fraction of irreversible capacities at 10 °C.

Overall, the low irreversible capacity losses of the NMC622 cathode confirm its good cycling stability under these operating conditions.[52,53] However, a notable capacity loss in the anode due to LLI during long-term cycling without Li plating results in higher anode potentials. This can lead to a phenomenon known as voltage slipping, which increases the cathode potentials to maintain the full cell voltage.[17,18] The higher cathode voltage can then contribute to additional aging effects.[18,52]

Post-mortem analysis.—As part of the post-mortem analysis of selected cells, the thickness of the harvested and washed electrodes was measured. Figure 8 illustrates the thickness of the double-side coated pristine anodes with different Si contents for the anodes from cells after formation and after aging at 35 °C, 10 °C, and 0 °C. The standard deviation of six measurements taken across the electrode is used to determine the error. The thickness of pristine electrodes and electrodes after the formation exhibit a high degree of homogeneity, as indicated by the low error values.

The pristine anodes demonstrate the trend of the decreasing thickness with increasing Si content for a constant areal capacity.[2] An initial irreversible swelling is already observed during formation, with the thickness of the electrodes after formation exhibiting a slight increase. A higher Si content leads to a more pronounced thickness increase due to volumetric changes of the Si compound and the increased amount of electrolyte decomposition products.[9] Consequently, the effect of the Si content on the anode thickness is less pronounced after the formation compared to the pristine anodes.

The irreversible swelling continues during aging. Graphite electrodes exhibited a 17 % increase in thickness, whereas the SiG20.8 electrode exhibited a 82 % increase after aging at 35 °C, reaching approximately 80 % SOH. The observed increase in thickness of the SiG3.0 and SiG5.8 anodes, at 43 % and 58 %, respectively, is consistent with the trend of greater thickness increase with higher Si content. This further corroborates the previous section's findings regarding the increasing fraction of LAAM in the total degradation of cells with increasing Si content in the anode. Interestingly, after aging at 35 °C, the anodes of all Si contents and graphite show thicknesses in a similar range.

The thickest electrodes were found for the graphite cells after aging at 0 °C and 10 °C. This can be attributed to the presence of a thick layer of metallic Li on the surface of the anode, as observed during the cell opening. The SiG20.8 cell exhibited local Li depositions in both the 0 °C and 10 °C aged cells, but no area-wide plating layer. In contrast, the SiG3.0 and SiG5.8 cells exhibited an inhomogeneous layer of plated Li only after 0 °C aging, resulting in a thickness increase with a large error value in Fig. 8.

It is noteworthy that there is no straightforward correlation between the number of cycles and the thickness increase when comparing different aging temperatures. For instance, the thickness increase of the SiG3.0 cell after 35 °C aging is considerably more pronounced compared to 10 °C, despite the number of cycles being almost twice as high at 10 °C. As previously mentioned in relation to the higher proportion of LAAM for the 35 °C cell, this could be a result of the increased usage of the Si component with increasing temperature.

Selected electrodes from the cell opening were utilized to prepare ion milling cross-sections for investigations via SEM and EDX in order to gain information about the structural and compositional changes occurring within the electrodes after cycling. The impact of aging at varying temperatures is shown in Fig. 9 for the SiG5.8 anode. Furthermore, the influence of the Si content in the anode after aging at 35 °C is shown in Fig. 10. The first columns in Figs. 9 and 10 (subfigures (a), (e), (i), (m)) display the SEM cross-section of the upper side of the electrode, with the copper current collector visible at the bottom. A yellow box marks the area, which is displayed magnified in the second column (subfigures (b), (f), (j), (n)). The bright particles in the SEM measurements are related to Si, while the dark particles are carbon/graphite. It is important to note that the visible Si particles in the size of several µm are in turn composed of

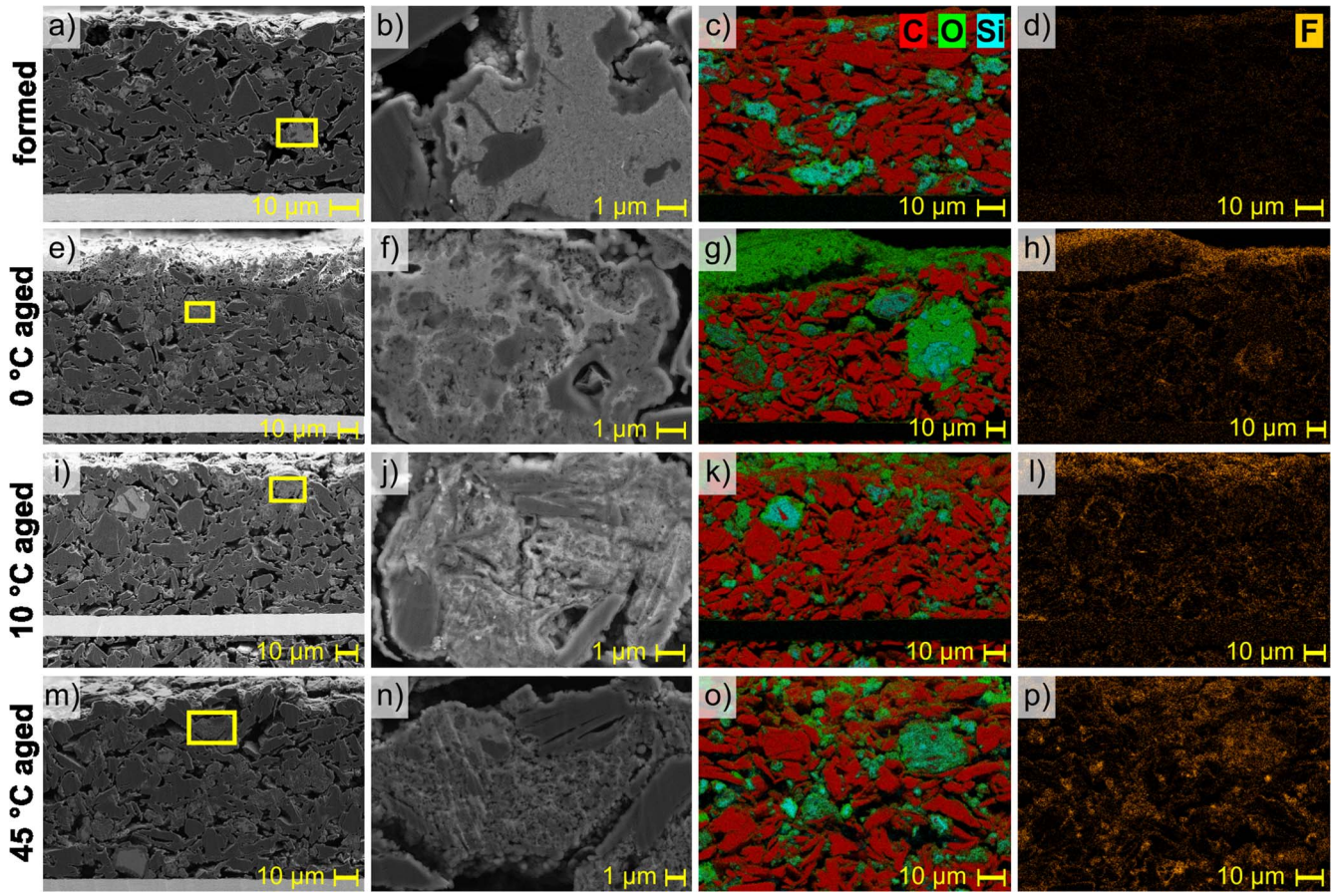

Figure 9. Cross-sectional SEM images (first and second column) and EDX elemental mappings (third and fourth column) for the SiG5.8 anode after the formation (a)–(d) and after the aging at (e)–(h) 0 °C, (i)–(l) 10 °C, and (m)–(p) 45 °C. The yellow box in the first column marks the area that is magnified in the second column. The third column displays the EDX mapping of C (red), O (green), and Si (blue), while the fourth column shows the EDX mapping of the same image section for F (orange).

nm-Si particles and carbon. The nano-size of the Si particles is most likely the reason why we do not observe strong cracks of the Si compound after aging.

The structural integrity of the electrodes undergoes notable changes with cyclic aging, as evidenced by the comparative analysis of the SEM images of the electrodes after formation (Fig. 9a) and those that have undergone aging at different temperatures (Figs. 9e, 9i, 9m). The electrode of the new cell after formation exhibits a compact structure. In the case of the electrode aged at 0 °C (Fig. 9e), a layer of deposited Li can be observed on the surface. The electrode itself exhibits slight structural loosening compared to an unaged electrode, but less so than those subjected to 10 °C and especially 45 °C aging conditions. The total pore volume appears to be nearly constant or slightly increased although the total thickness has increased. This is consistent with the observed thickening of the electrodes in Fig. 8.

Similarly, the structure of the secondary Si particles exhibits a notable transformation from a dense and homogenous structure in the new state, as visible in Fig. 9b, to a loose and inhomogeneous structure with nanoscale pores in the aged state. This could have been contributed to the increasing electrode thickness. It further appears that the carbon coating around the Si secondary particles still persists in the aged state. Once more, the 0 °C aged Si particles appear to be less affected than the 10 °C and 45 °C aged ones. This is in accordance with the other results indicating that degradation at 0 °C is dominated by Li plating with minor LAAM. However, due to the limited resolution of the SEM, the SEI growth, which is likely occurring at the surface of the nm-scale primary Si particles, cannot be detected here.[16]

As illustrated in the first column of Fig. 10 (subfigures (a), (e), (I), (m)), there is a notable trend of increasing loss of the electrode's structural integrity in the aged state with elevated Si content in the anode. Of particular note is the SiG20.8 electrode (Fig. 10m), which exhibits a substantial crack that runs parallel to the current collector. Although the crack could have also occurred during cell opening or cross-section preparation, the crack is evidence of the fragility of the electrode with high Si content. Such cracks have the potential to result in the loss of electrical contact between particles, which could ultimately result in LAAM. A more detailed examination of the Si secondary particles in the second column of Fig. 10 (subfigures (b), (f), (j), (n)) reveals a more pronounced impact of cycling and a more porous structure in the secondary particle with increasing Si content in the anode. Additionally, the carbon shell encasing the Si primary particles also appears to have remained in the aged state even at the highest Si content, as observed in Fig. 10n.

The EDX elemental mappings for carbon (C), oxygen (O), Si, and fluoride (F) in the third and fourth columns of Figs. 9 and 10 can provide further insights into the aging mechanism. Due to exposure of the samples to air, statements on O are limited. Nevertheless, the elemental distributions of O and Si exhibit a high degree of correlation, as evidenced by the increasing O content in the anodes with increasing Si content in the third column of Fig. 10. As illustrated in the third column of Fig. 9, the amount of O tends to increase further in the aged state. However, the substantially elevated O amount in Fig. 9g is associated with the plated metallic Li, which has reacted with oxygen from the ambient air during cross-section preparation. The presence of Li plating on the anode surface is fully consistent with results of various other methods.[39,40]

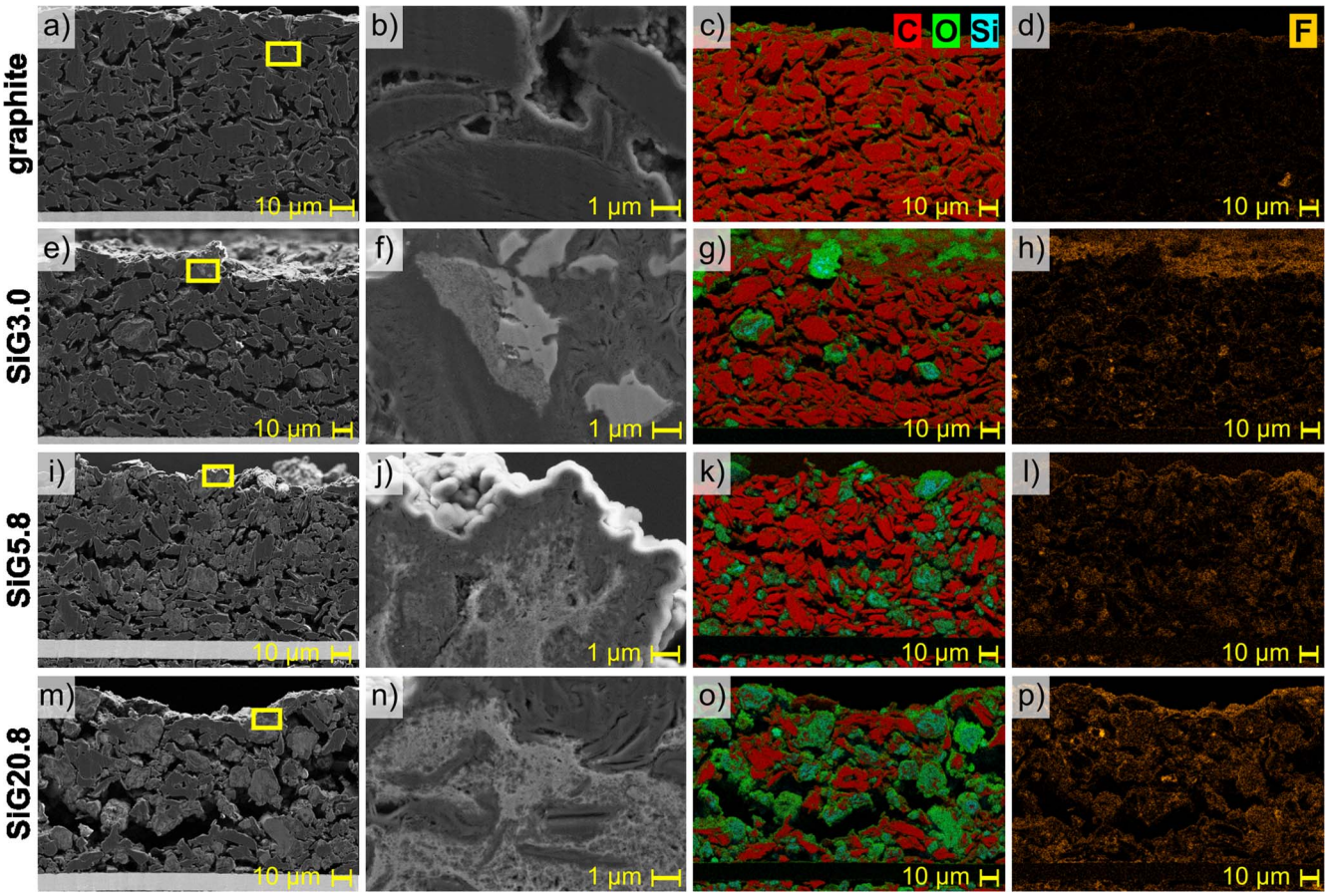

Figure 10. Cross-sectional SEM images (first and second column) and EDX elemental mappings (third and fourth column) for anodes with different Si content: (a)–(d) graphite, (e)–(f) SiG3.0, (i)–(l) SiG5.8, and (m)–(p) SiG20.8 after aging at 35 °C. The yellow box in the first column marks the area that is magnified in the second column. The third column displays the EDX mapping of C (red), O (green), and Si (blue), while the fourth column shows the EDX mapping of the same image section for F (orange).

A further notable correlation is observed between the elemental distribution of F, O, and Si in both Figs. 9 and 10. The anode of the new cell (Fig. 9d) has a very small amount of F and O, which significantly increases in the aged cells, with the greatest extent observed in the 45 °C aged cell (Fig. 9p). Both F and O are typical components of the SEI in Si containing cells.[16,20,35,48,85,86] The FEC-containing electrolyte increases the F amount and simultaneously reduces the O amount.[48] This is evident in the fourth column of Fig. 10, particularly when comparing the graphite cell (Fig. 10d) without FEC electrolyte additive and the other cells with FEC additive (Figs. 10h, 10l, 10p). Furthermore, the increasing amount of F with increasing Si content is clearly observable. This is consistent with Li et al. who observed a considerable increase in the F content on Si particles in aged anodes, reaching approximately five times the level observed in new cells, due to the extensive growth of the SEI.[87] This indicates that although the cell ages as a consequence of electrolyte decomposition, this process is initiated by the silicon component.

Additional elemental mappings were conducted for the transition metals nickel (Ni) and manganese (Mn), as dissolution and subsequent deposition of transition metals on the anode is a well-known aging mechanism in Li-ion batteries.[41,44,88] However, for all aged cells, only very small quantities of Ni and Mn were identified in the anode, confirming the stability of the cathode which is consistent with the discussion above.

Conclusions

This study examined the cyclic aging across a wide temperature range from −10 °C up to 55 °C of a hundred pouch full cells containing Si-graphite composite anodes, with Si-contents varying from 0 wt% to 20.8 wt%. To ensure comparability, the anodes had been designed with similar areal capacity, porosity, and tortuosity, whereas the cells had very similar N/P ratios. The constant areal capacities of the anodes resulted in thinner anode coatings with higher Si contents. The NMC622 cathode being used demonstrated high stability with very small aging effects, which makes it possible to assign the observed main aging effects to the anode.

Our investigations reveal that the temperature dependent performance of new cells varies significantly with the Si content in the anode. While the capacity at high temperatures was similar across all cells with different Si contents in the anode, notable differences emerged already at 25 °C and 0.5 C. This discrepancy was most pronounced at 0 °C, where the graphite cells delivered only 74 % of the rated capacity, whereas the SiG20.8 cells delivered 87 %. A higher Si content in the anode resulted in higher anode potentials and thinner electrodes with lower resistance, which was particularly beneficial at low temperatures reducing overpotentials and enhancing energy efficiency.

Temperature dependent degradation and cyclic aging rates varied significantly with Si contents. Cells with a graphite-only anode demonstrated the highest cycling stability, reaching EOL at 80 % SOH after over 3,000 cycles at 0.5 C, while cells with 20.8 wt% Si in the anode only lasted around 200 cycles. Post-mortem analyses revealed increased LAAM and substantial SEI growth, particularly in cells with high Si content in the anode aged at 35 °C. This was confirmed by increased anode thickness, less reversible capacity in reconstructed half cells, and higher amounts of F and O on aged negative electrodes with higher Si content. Thus, similar to calendar aged cells,[16] the Si-component is a lifetime limiting factor.

Parasitic side reactions such as the SEI growth accelerate at higher temperatures, following an Arrhenius law for the cyclic aging rate. The activation energies observed for cells with pure graphite up to a medium Si content in the composite anodes were found to be similar, indicating the presence of consistent degradation mechanisms. In contrast, a reduced temperature dependence in the low and high temperature ranges was observed for the highest Si content in the anode, suggesting the presence of additional aging mechanisms that are not dependent on temperature.

At low temperatures, Li plating, which increases the aging rate with decreasing temperature, is the dominating aging mechanisms. The optimum cycling temperature for the longest cycle life occurs at the lowest temperature without Li plating. This was found to be 30 °C for the graphite cell, decreasing to 10 °C for cells with a low Si content in the anode. Measurements of the anode potential vs Li/Li^+ confirm this trend of decreasing Li plating onset temperatures with increasing Si content. Interestingly, for cells with 20.8 wt% Si, the optimum temperature increased again to 25 °C. However, these cells showed the lowest aging rate at temperatures below 0 °C, indicating superior low temperature performance and longer cycle life for cell with high Si content in the anode. The better low temperature performance and aging rate of the cells with Si compound is due to (i) an increase of the minimum anode potential, (ii) the thinner anode coatings, (iii) the reduced utilization of the Si component at low temperatures.

At low temperatures, decreased utilization of the Si component reduces the volume expansion during lithiation, enhancing the long-term stability. This is further confirmed by a less strong anode thickness increase at lower temperatures. However, increasing the Si content further is unlikely to extend cycle life due to more pronounced LAAM.

In conclusion, the results emphasize the necessity of carefully optimizing the anode's Si content based on the intended operating temperature range of the battery. Even small amounts of Si (<6 wt %) significantly alter performance and cyclic aging behavior of the anode and therefore also of the battery cell itself. A higher Si content can be particularly beneficial for low temperature performance but is detrimental for high temperature applications. Therefore, a balanced Si content in the anode in the range of a few wt% seems to be the best compromise in achieving optimal performance across different temperatures. When scaling these findings to larger cells, the more pronounced heating behavior during operation and potential electrolyte depletion due to extensive SEI growth, especially in cells with high Si content, must be considered additionally.

Acknowledgments

We gratefully acknowledge the German Federal Ministry of Education and Research (BMBF) for financial support of the project CharLiSiKo (03XP0333A) within the AQua cluster as well as project management by the Projektträger Jülich (PTJ). The authors would like to thank the ZSW members M. Flügel, C. Hogrefe, and K. Bischof for helpful discussions, as well as C. Pfeifer for SEM/EDX measurements.

ORCID

Max Feinauer https://orcid.org/0000-0003-2483-8257
Margret Wohlfahrt-Mehrens https://orcid.org/0000-0002-5118-5215
Markus Hölzle https://orcid.org/0009-0004-8278-1089
Thomas Waldmann https://orcid.org/0000-0003-3761-1668

References

1. C. Berg, R. Morasch, M. Graf, and H. A. Gasteiger, *J. Electrochem. Soc.*, **170**, 30534 (2023).
2. M. Flügel, M. Bolsinger, M. Marinaro, V. Knoblauch, M. Hölzle, M. Wohlfahrt-Mehrens, and T. Waldmann, *J. Electrochem. Soc.*, **170**, 60536 (2023).
3. P. Li, H. Kim, S-T. Myung, and Y-K. Sun, *Energy Storage Mater.*, **35**, 550 (2021).
4. M. Weiss et al., *Adv. Energy Mater.*, **11**, 2101126 (2021).
5. J. Asenbauer, T. Eisenmann, M. Kuenzel, A. Kazzazi, Z. Chen, and D. Bresser, *Sustainable Energy Fuels*, **4**, 5387 (2020).
6. S. Chae, S-H. Choi, N. Kim, J. Sung, and J. Cho, *Angew. Chem. Int. Ed.*, **59**, 110 (2020).
7. M. T. McDowell, S. W. Lee, W. D. Nix, and Y. Cui, *Adv. Mater.*, **25**, 4966 (2013).
8. L. Köbbing, A. Latz, and B. Horstmann, *Adv. Funct. Mater.*, **34**, 2308818 (2024).
9. M. Wetjen, S. Solchenbach, D. Pritzl, J. Hou, V. Tileli, and H. A. Gasteiger, *J. Electrochem. Soc.*, **165**, A1503 (2018).
10. S. He, S. Huang, S. Wang, I. Mizota, X. Liu, and X. Hou, *Energy Fuels*, **35**, 944 (2021).
11. X. Zhang, J. Weng, C. Ye, M. Liu, C. Wang, S. Wu, Q. Tong, M. Zhu, and F. Gao, *Materials*, **15**, 4264 (2022).
12. J. Lyubina, *Appl. Phys. Lett.*, **118**, 090501 (2021).
13. N. Kim, Y. Kim, J. Sung, and J. Cho, *Nat. Energy*, **8**, 921 (2023).
14. P. Heugel, W. Märkle, T. Deich, O. von Kessel, and J. Tübke, *Journal of Energy Storage*, **53**, 105101 (2022).
15. A. Pfrang, A. Kersys, A. Kriston, R-G. Scurtu, M. Marinaro, and M. Wohlfahrt-Mehrens, *J. Electrochem. Soc.*, **170**, 30548 (2023).
16. K. Bischof, M. Flügel, M. Hölzle, M. Wohlfahrt-Mehrens, and T. Waldmann, *J. Electrochem. Soc.*, **171**, 10510 (2024).
17. K. Kalaga, M-T. F. Rodrigues, S. E. Trask, I. A. Shkrob, and D. P. Abraham, *Electrochim. Acta*, **280**, 221 (2018).
18. M-T. F. Rodrigues, J. A. Gilbert, K. Kalaga, and D. P. Abraham, *J. Phys.: Energy*, **2**, 24002 (2020).
19. J. D. McBrayer et al., *Nat. Energy*, **6**, 866 (2021).
20. K. Richter, T. Waldmann, M. Kasper, C. Pfeifer, M. Memm, P. Axmann, and M. Wohlfahrt-Mehrens, *J. Phys. Chem. C*, **123**, 18795 (2019).
21. M. Flügel, K. Richter, M. Wohlfahrt-Mehrens, and T. Waldmann, *J. Electrochem. Soc.*, **169**, 50533 (2022).
22. S. Bazlen, P. Heugel, O. von Kessel, W. Commerell, and J. Tübke, *Journal of Energy Storage*, **49**, 104044 (2022).
23. K. P. C. Yao, J. S. Okasinski, K. Kalaga, J. D. Almer, and D. P. Abraham, *Adv. Energy Mater.*, **9**, 1803380 (2019).
24. G. G. Eshetu, H. Zhang, X. Judez, H. Adenusi, M. Armand, S. Passerini, and E. Figgemeier, *Nat. Commun.*, **12**, 5459 (2021).
25. C. Heubner, T. Liebmann, O. Lohrberg, S. Cangaz, S. Maletti, and A. Michaelis, *Batteries & Supercaps*, **5**, e202100182 (2022).
26. M. P. Bonkile, Y. Jiang, N. Kirkaldy, V. Sulzer, R. Timms, H. Wang, G. Offer, and B. Wu, *J. Power Sources*, **606**, 234256 (2024).
27. N. Kirkaldy, M. A. Samieian, G. J. Offer, M. Marinescu, and Y. Patel, *ACS Appl. Energy Mater.*, **5**, 13367 (2022).
28. A. Mikheenkova, A. J. Smith, K. B. Frenander, Y. Tesfamhret, N. R. Chowdhury, C-W. Tai, T. Thiringer, R. W. Lindström, M. Hahlin, and M. J. Lacey, *J. Electrochem. Soc.*, **170**, 80503 (2023).
29. L. de Sutter, G. Berckmans, M. Marinaro, J. Smekens, Y. Firouz, M. Wohlfahrt-Mehrens, J. van Mierlo, and N. Omar, *Energies*, **11**, 2948 (2018).
30. L. Wildfeuer, A. Karger, D. Aygül, N. Wassiliadis, A. Jossen, and M. Lienkamp, *J. Power Sources*, **560**, 232498 (2023).
31. K. Richter, T. Waldmann, N. Paul, N. Jobst, R-G. Scurtu, M. Hofmann, R. Gilles, and M. Wohlfahrt-Mehrens, *Chem. Sus. Chem*, **13**, 529 (2020).
32. M. Schindler, J. Sturm, S. Ludwig, A. Durdel, and A. Jossen, *J. Electrochem. Soc.*, **168**, 60522 (2021).
33. S. Dhillon, G. Hernández, N. P. Wagner, A. M. Svensson, and D. Brandell, *Electrochim. Acta*, **377**, 138067 (2021).
34. E. Moyassari, T. Roth, S. Kücher, C-C. Chang, S-C. Hou, F. B. Spingler, and A. Jossen, *J. Electrochem. Soc.*, **169**, 10504 (2022).
35. T. Vorauer et al., *Commun Mater*, **4**, 1 (2023).
36. P. Bernard, J. P. Alper, C. Haon, N. Herlin-Boime, and M. Chandesris, *J. Power Sources*, **435**, 226769 (2019).
37. F. Holtstiege, P. Bärmann, R. Nölle, M. Winter, and T. Placke, *Batteries*, **4**, 4 (2018).
38. K. Sun, X. Li, Z. Zhang, K. Fu, X. Xiao, L. Gong, and P. Tan, *Energy Storage Mater.*, **66**, 103216 (2024).
39. T. Waldmann, B-I. Hogg, and M. Wohlfahrt-Mehrens, *J. Power Sources*, **384**, 107 (2018).
40. T. Waldmann et al., *J. Electrochem. Soc.*, **171**, 70526 (2024).
41. T. Waldmann, M. Wilka, M. Kasper, M. Fleischhammer, and M. Wohlfahrt-Mehrens, *J. Power Sources*, **262**, 129 (2014).
42. X-G. Yang and C-Y. Wang, *J. Power Sources*, **402**, 489 (2018).
43. G. Kucinskis, M. Bozorgchenani, M. Feinauer, M. Kasper, M. Wohlfahrt-Mehrens, and T. Waldmann, *J. Power Sources*, **549**, 232129 (2022).
44. M. Feinauer, M. Wohlfahrt-Mehrens, M. Hölzle, and T. Waldmann, *J. Power Sources*, **594**, 233948 (2024).
45. M. Feinauer, A. A. Abd-El-Latif, P. Sichler, A. Aracil Regalado, M. Wohlfahrt-Mehrens, and T. Waldmann, *J. Power Sources*, **570**, 233046 (2023).
46. M. Bozorgchenani, G. Kucinskis, M. Wohlfahrt-Mehrens, and T. Waldmann, *J. Electrochem. Soc.*, **169**, 30509 (2022).
47. A. Friesen, X. Mönnighoff, M. Börner, J. Haetge, F. M. Schappacher, and M. Winter, *J. Power Sources*, **342**, 88 (2017).
48. M. J. Piernas-Muñoz, Z. Yang, M. Kim, S. E. Trask, A. R. Dunlop, and I. Bloom, *J. Power Sources*, **487**, 229322 (2021).
49. M. J. Piernas-Muñoz, S. E. Trask, A. R. Dunlop, E. Lee, and I. Bloom, *J. Power Sources*, **441**, 227080 (2019).
50. R. Bednorz and T. Gewald, *Batteries*, **6**, 34 (2020).
51. C. Hogrefe et al., *J. Electrochem. Soc.*, **171**, 70503 (2024).
52. R. Jung, M. Metzger, F. Maglia, C. Stinner, and H. A. Gasteiger, *J. Electrochem. Soc.*, **164**, A1361 (2017).
53. H-J. Noh, S. Youn, C. S. Yoon, and Y-K. Sun, *J. Power Sources*, **233**, 121 (2013).

54. E. Markevich, G. Salitra, and D. Aurbach, *ACS Energy Lett.*, **2**, 1337 (2017).
55. C. Xu, F. Lindgren, B. Philippe, M. Gorgoi, F. Björefors, K. Edström, and T. Gustafsson, *Chem. Mater.*, **27**, 2591 (2015).
56. E. Markevich, G. Salitra, and D. Aurbach, *J. Electrochem. Soc.*, **163**, A2407 (2016).
57. W. Wang and S. Yang, *J. Alloys Compd.*, **695**, 3249 (2017).
58. D. J. Arnot, E. Allcorn, and K. L. Harrison, *J. Electrochem. Soc.*, **168**, 110509 (2021).
59. T. Jaumann et al., *Energy Storage Mater.*, **6**, 26 (2017).
60. J. C. Burns, R. Petibon, K. J. Nelson, N. N. Sinha, A. Kassam, B. M. Way, and J. R. Dahn, *J. Electrochem. Soc.*, **160**, A1668 (2013).
61. K. Xu, *Chem. Rev.*, **114**, 11503 (2014).
62. T. Waldmann, B-I. Hogg, M. Kasper, S. Grolleau, C. G. Couceiro, K. Trad, B. P. Matadi, and M. Wohlfahrt-Mehrens, *J. Electrochem. Soc.*, **163**, A1232 (2016).
63. M. Alipour, C. Ziebert, F. V. Conte, and R. Kizilel, *Batteries*, **6**, 35 (2020).
64. B. Liu, B. Li, and S. Guan, *Electrochem. Solid-State Lett.*, **15**, A77 (2012).
65. O. Yariv, D. Hirshberg, E. Zinigrad, A. Meitav, D. Aurbach, M. Jiang, and B. R. Powell, *J. Electrochem. Soc.*, **161**, A1422 (2014).
66. I. Zilberman, J. Sturm, and A. Jossen, *J. Power Sources*, **425**, 217 (2019).
67. J. Guo, Y. Li, J. Meng, K. Pedersen, L. Gurevich, and D-I. Stroe, *Journal of Energy Chemistry*, **74**, 34 (2022).
68. M. Broussely, S. Herreyre, P. Biensan, P. Kasztejna, K. Nechev, and R. J. Staniewicz, *J. Power Sources*, **97-98**, 13 (2001).
69. L. de Sutter, G. Berckmans, M. Marinaro, M. Wohlfahrt-Mehrens, M. Berecibar, and J. van Mierlo, *J. Power Sources*, **451**, 227774 (2020).
70. Z. Yang, S. E. Trask, X. Wu, and B. J. Ingram, *Batteries*, **9**, 138 (2023).
71. M. Haruta, T. Okubo, Y. Masuo, S. Yoshida, A. Tomita, T. Takenaka, T. Doi, and M. Inaba, *Electrochim. Acta*, **224**, 186 (2017).
72. L. Liao, P. Zuo, Y. Ma, Y. An, G. Yin, and Y. Gao, *Electrochim. Acta*, **74**, 260 (2012).
73. S. Käbitz, J. B. Gerschler, M. Ecker, Y. Yurdagel, B. Emmermacher, D. André, T. Mitsch, and D. U. Sauer, *J. Power Sources*, **239**, 572 (2013).
74. B. Y. Liaw, E. Roth, R. G. Jungst, G. Nagasubramanian, H. L. Case, and D. H. Doughty, *J. Power Sources*, **119-121**, 874 (2003).
75. B-I. Hogg, T. Waldmann, and M. Wohlfahrt-Mehrens, *J. Electrochem. Soc.*, **167**, 90525 (2020).
76. C. Hogrefe, M. Hölzle, M. Wohlfahrt-Mehrens, and T. Waldmann, *J. Electrochem. Soc.*, **170**, 110535 (2023).
77. Y. Xiao, R. Xu, C. Yan, J-Q. Huang, Q. Zhang, and M. Ouyang, *Adv. Funct. Mater.*, **32**, 2108449 (2022).
78. C. Hogrefe, T. Waldmann, M. B. Molinero, L. Wildner, P. Axmann, and M. Wohlfahrt-Mehrens, *J. Electrochem. Soc.*, **169**, 50519 (2022).
79. T. Waldmann, J. B. Quinn, K. Richter, M. Kasper, A. Tost, A. Klein, and M. Wohlfahrt-Mehrens, *J. Electrochem. Soc.*, **164**, A3154 (2017).
80. M. Petzl and M. A. Danzer, *J. Power Sources*, **254**, 80 (2014).
81. M. C. Smart and B. V. Ratnakumar, *J. Electrochem. Soc.*, **158**, A379 (2011).
82. P. Keil, S. F. Schuster, J. Wilhelm, J. Travi, A. Hauser, R. C. Karl, and A. Jossen, *J. Electrochem. Soc.*, **163**, A1872 (2016).
83. J. Schmitt, M. Schindler, A. Oberbauer, and A. Jossen, *J. Power Sources*, **532**, 231296 (2022).
84. T. Waldmann et al., *J. Electrochem. Soc.*, **163**, A2149 (2016).
85. B. Philippe, R. Dedryvère, J. Allouche, F. Lindgren, M. Gorgoi, H. Rensmo, D. Gonbeau, and K. Edström, *Chem. Mater.*, **24**, 1107 (2012).
86. B. Philippe, R. Dedryvère, M. Gorgoi, H. Rensmo, D. Gonbeau, and K. Edström, *Chem. Mater.*, **25**, 394 (2013).
87. X. Li, A. M. Colclasure, D. P. Finegan, D. Ren, Y. Shi, X. Feng, L. Cao, Y. Yang, and K. Smith, *Electrochim. Acta*, **297**, 1109 (2019).
88. J. Wang, J. Purewal, P. Liu, J. Hicks-Garner, S. Soukazian, E. Sherman, A. Sorenson, L. Vu, H. Tataria, and M. W. Verbrugge, *J. Power Sources*, **269**, 937 (2014).